Corrosion behavior of a ZrCN coated Ti alloy with potential application as a bipolar plate for proton exchange membrane fuel cell

Jiang Xu [a, b, *], Hao Jie Huang [a], ZhengYang Li [c], Song Xu [d], Hongliang Tao [e], Paul Munroe [d], Zong-Han Xie [b, f, **]

[a] Department of Material Science and Engineering, Nanjing University of Aeronautics and Astronautics, 29 Yudao Street, Nanjing 210016, PR China
[b] School of Mechanical & Electrical Engineering, Wuhan Institute of Technology, 693 Xiongchu Avenue, Wuhan 430073, PR China
[c] Institute of Mechanics, Chinese Academy of Sciences, Beijing 100190, PR China
[d] School of Materials Science and Engineering, University of New South Wales, NSW 2052, Australia
[e] Guangdong Monte-bianco New Materials Co., Ltd., Foshan 528313, PR China
[f] School of Mechanical Engineering, University of Adelaide, SA 5005, Australia

ARTICLE INFO

ABSTRACT

To improve the corrosion resistance, surface electrical conductivity and wettability of Ti−6Al−4V used in polymer electrolyte membrane fuel cell (PEMFC), a ZrCN nanocrystalline coating was deposited on Ti−6Al−4V substrate using double cathode glow discharge technique. The new coating exhibited a nanocomposite structure, consisting of amorphous C, CN_x and nanocrystalline ZrCN. The effect of the HF concentrations on the corrosion behavior of the coating was investigated by potentiodynamic, potentiostatic polarizations and electrochemical impedance spectroscopy (EIS) in a simulated the operating conditions of a PEMFC. With increasing HF concentrations, the corrosion potential (E_{corr}) decreased and the corrosion current density (i_{corr}) of the ZrCN coating increased, indicating that corrosion resistance decreased with the increase of HF concentrations. However, at any given concentration of HF, the corrosion resistance of the ZrCN coating was significantly higher than that of uncoated Ti−6Al−4V. The results of EIS measurements showed that with increasing the concentration of HF, the resistance of the passive film (R_b) formed on the ZrCN coating decreased slightly, being of the order of magnitude of ~10^7 Ω cm^2, which was an improvement by four orders of magnitude compared to uncoated Ti-6A1-4V. At a compaction force of 140 N cm^{-2}, no perceptible difference in the interfacial contact resistance (ICR) of ZrCN-coated Ti-6A1-4V was observed before and after potentiostatic polarization for 120 min, and its ICR values were reduced by one order of magnitude in comparison to that of uncoated Ti-6A1-4V. Moreover, ZrCN-coated Ti-6A1-4V exhibited a much low surface wettability than uncoated Ti−6Al−4V alloy, which was beneficial for both water management and improving corrosion resistance.

1. Introduction

There are rising concerns about the environmental and heath impact of the use of fossil fuels. As a consequence, much attention has recently been devoted to the development of more efficient and cleaner technologies. Fuel cells are environmentally friendly energy generation devices, which convert chemical energy directly into electrical energy with high efficiency and virtual zero-emissions [1]. Among the various fuel cells under development, polymer electrolyte membrane fuel cells (PEMFCs) are regarded as one of the most promising power sources for residential and transportation applications due to their high power density, low operating temperature, and rapid start-up [2]. A typical PEM fuel cell comprises membrane electrode assemblies (MEAs), gas diffusion layers (GDLs) and bipolar plates. Among the components of PEMFCs, the bipolar plates are the most bulky and also one of the

* Corresponding author. Department of Material Science and Engineering, Nanjing University of Aeronautics and Astronautics, 29 Yudao Street, Nanjing 210016, PR China.
** Corresponding author. School of Mechanical & Electrical Engineering, Wuhan Institute of Technology, 693 Xiongchu Avenue, Wuhan 430073, PR China.
E-mail addresses: xujiang73@nuaa.edu.cn (J. Xu), zonghan.xie@adelaide.edu.au (Z.-H. Xie).

most expensive to manufacture. These plates play multiple roles in the long-term operation of the fuel cell, including feeding the fuel and air to a gas diffusion layer-electrodes assembly, managing heat and water flow, and providing the electrical contact between adjacent cells [3]. Currently, the high cost and the large mass of these components are considered to be a major barrier to the commercial application of PEFC fuel cells [4]. Hence, the reduction of the cost, mass, and volume of these bipolar plates is critical to the development of PEMFCs. For practical application, bipolar plate materials should possess high corrosion resistance, high electrical conductivity, and low permeability and be economic to manufacture [5]. Traditionally, bipolar plates are made from non-porous graphite, because of its good electronic conductivity and high chemical stability in PEM fuel cell environments. However, its low toughness, gas permeability and the difficulties in machining gas flow channels increase fabrication costs and the overall size of a PEFC stack [6]. In lieu of this, considerable effort has been made into the development of metallic bipolar plates, from materials such as stainless steel and titanium and aluminum alloys [7,8]. Compared with stainless steels, titanium alloys not only exhibit a higher corrosion resistance in highly acidic and humid conditions, but also have a higher specific strength, and thereby high volumetric and gravimetric power densities, particularly suitable for portable PEM systems [3]. Unfortunately, metallic bipolar plates are highly vulnerable to corrosive attack in the strong acidic operating environment of the electrolyte membrane where the pH level is 2–3 [9]. The resultant metal ions, e.g. Fe, Cr and Ni ions, released from metallic bipolar plates can degrade the membrane performance and poison the electrode catalysts [10]. Moreover, the formation of passive films formed on the metallic bipolar plates lead to an increase in the interfacial contact resistance between their surface and gas diffusion layers, and this adversely impacts cell performance due to an increase in the potential loss. To address this drawback, various types of coatings, such as gold [11], amorphous carbon (a-C) films [12], nitrogen plasma-implanted surface layers [13], iridium oxide (IrO_2) and platinum layers [14] fabricated onto titanium substrates by different surface modification techniques, have been investigated to protect uncoated titanium from the harsh operating environment. Refractory metal nitrides and carbonitrides coatings have extensive applications as coating materials, ranging from hard and protective coatings on mechanical tools, wear resistant and decorative layers on optical components, to diffusion barriers in microelectronic industry, because of their unusual combination of physical and chemical properties [15]. Among the large refractory metal carbonitrides, ZrCN is an attractive material because of its excellent chemical and physical properties, such as relatively low electrical resistivity and high corrosion resistance [16]. For instance, Cotrut et al. [17] reported that $ZrC_{1-x}N_x$ deposited by magnetron sputtering could both improve the corrosion resistance and reduce the friction coefficient of Ti–6Al–4V. To the best of our knowledge, there have been no reports available in the literature with regard to the use of ZrCN coatings for metallic bipolar plates. Furthermore, fluoride ion concentrations in anodic and cathodic media in PEM fuel cells varied within a small range, which could have a significant effect on the corrosion behavior of metallic bipolar plates [18]. In the current work, to investigate its potential application as a protective coating for PEMFC bipolar plates, a ZrCN nanocrystalline coating was deposited onto a Ti-6A1-4V substrate using a double glow discharge plasma technique. The effect of the concentration of HF additions on the corrosion behavior of the ZrCN coating was systematically investigated using various electrochemical methods in a simulated PEMFC environment. Furthermore, the interfacial contact resistance and surface wettability of the ZrCN-coated specimen were measured and compared with the uncoated Ti-6A1-4V alloy.

2. Experimental details

2.1. Preparation of ZrCN nanocrystalline coating

A ZrCN nanocrystalline coating was deposited onto a Ti-6A1-4V substrate using a stoichemetric ZrC target (99.9% in purity) by a double cathode glow discharge apparatus. In the process of double cathode glow discharge, one cathode serves as the target fabricated from the desired sputtering materials, and the other cathode as the substrate material, as described elsewhere [19]. When two different voltages are applied to the two cathodes, glow discharge occurs. A ZrC disk with dimensions $\Phi 80 \times 4$ mm used as the sputtering target was fabricated from ball-milled Zr (300 mesh, >99.9% purity) and C powders (graphite, 500 mesh, >99.9% purity) by employing cold compaction under a pressure of 600 MPa. Disk-shaped substrates, with dimensions $\Phi 40 \times 3$ mm, were machined from a commercial Ti–6Al–4V alloy rod. The nominal composition of this alloy in weight percent is: Al, 6.04; V, 4.03; Fe, 0.3; O, 0.1; C, 0.1; N, 0.05; H, 0.015 and the balance Ti. Before sputter deposition, the polished substrates were ultrasonically cleaned in acetone, alcohol, distilled water and then dried. During deposition, the working pressure was fixed at 35 Pa with an $Ar:N_2$ flux ratio of 10:1. The distance between the target and the substrate holder was fixed at 10 mm. The deposition temperature, measured by a thermocouple located near the sample, was held within the range of 600 ± 20 °C. The bias voltages of substrate and target electrodes were −350 and −750 V, respectively, and the deposition time was about 2 h.

2.2. Structural characterization and mechanical properties

The phase composition of the as-deposited coating was characterized using X-ray diffraction (XRD) (D8ADVANCE using Cu Kα radiation), with the instrument operating at 35 kV and 40 mA. X-ray data were collected using a 0.1° step scan with a count time of 1 s. The cross-sectional and corroded surface morphology of the as-deposited coatings were studied by scanning electron microscopy (SEM,Quanta200, FEI Company). Transmission electron microscopy (TEM) and high-resolution transmission electron microscopy (HRTEM) images were acquired using a JEOL JEM-2010 operating at an accelerating voltage of 200 kV. Thin-foil specimens for TEM observation were prepared by single-jet electropolishing from the untreated side of the substrate. All X-ray photoelectron spectroscopy (XPS) measurements were performed with a Kratos AXIS Ultra ESCA System using an Al Kα X-ray source with an energy of 1486.68 eV. The accelerating voltage and emission current of the X-ray source were kept at 13 kV and 12 mA, respectively. The base pressure of the sample analysis chamber was maintained at $\sim 10^{-10}$ Torr. The pass energy was selected to be 100 eV for survey scans and 20 eV for feature scans to ensure both high resolution and good sensitivity. After subtracting the background signal, the spectra were fitted by both Gaussian and mixed Gaussian/Lorentzian functions. Peak positions were then calibrated with respect to the C1s peak at 285 eV from hydrocarbon contamination. Peak identification was performed with reference to the NIST XPS database (V4.0).

A nanoindenter, equipped with a spherical diamond tip having a nominal radius of 5 mm, was used (UMIS 2000, CSIRO, Sydney, Australia) to evaluate the hardness of the as-deposited coating and uncoated Ti-6A1-4V substrate. The system has load and displacement resolutions of 10 μN and 1 nm, respectively. Fused silica was used as a standard sample for tip calibration. The indentation was performed by driving the indenter at a constant loading rate of 40 mN min^{-1} into the material surface with the maximum applied load of 20 mN, which is less than 10% of the coating thickness. The standard analysis procedure proposed by Oliver and Pharr [20] was
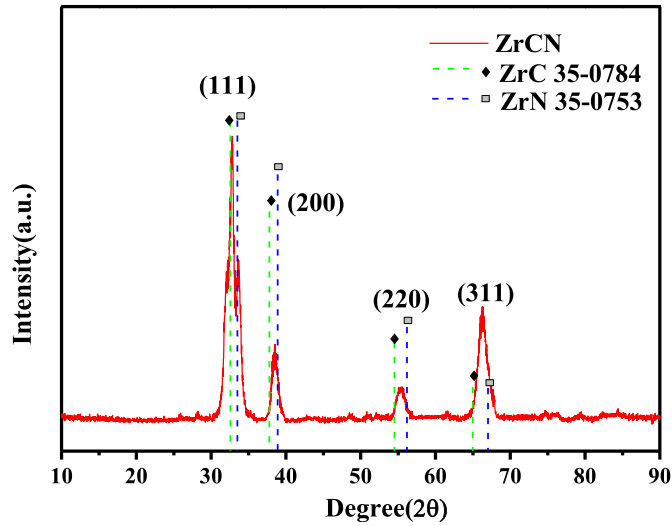
Fig. 1. Typical X-ray diffraction patterns recorded from the as-deposited ZrCN coating.

used to determine the hardness of the specimens from the unloading curve. For each sample, nanoindentation was conducted for five indentations to ensure the repeatability of the experimental data.

2.3. Electrochemical measurements

Electrochemical measurements were evaluated in 0.5 M H_2SO_4 solution containing different HF concentrations (namely, 2, 4 and 6 ppm, corresponding to pH values of 1.4, 1.3 and 1.2) maintained at 70 °C to simulate the aggressive environment typical of PEMFCs,

using a CHI660C electrochemical workstation. A standard three-compartment cell was used with a working electrode, a platinum sheet as the counter electrode and a saturated calomel electrode (SCE) insulated with a Luggins capillary to avoid chloride contamination as a reference electrode. Throughout this paper, all electrode potentials were referred to the SCE. The potentiodynamic current−potential curves were recorded at a sweep rate of 20 mV min^{-1}Prior to and during the electrochemical measurements, the solution was purged with either hydrogen (99.99% purity) or air, to simulate either the anodic or cathodic PEMFCs environments, respectively. Potentiostatic polarization measurements were carried out for 2.5 h at −0.1 V_{SCE} for the anode and +0.6 V_{SCE} for the cathode environment. EIS measurement started after stabilization for about 1 h at an open-circuit potential (OCP). The frequency was swept from 100 kHz down to 10 mHz, with an acquisition of 12 points per decade of frequency and an amplitude of the AC signal of 10 mV.

2.4. Interfacial contact resistance (ICR) and contact angle measurements

Interfacial contact resistance (ICR) values of the uncoated and ZrCN coated Ti−6Al−4V were determined using methods described in detail elsewhere [21]. In this experimental setup, two pieces of conductive carbon paper (Toray TGP-H-090) were sandwiched between the sample and two copper plates that were plated with gold on both sides to increase conductivity. A constant electrical current of 0.5 A was applied via the two copper plates and the variation in the total voltage was recorded as a function of steadily increasing compaction force up to 260 Ncm^{-2}. The resistance of the carbon paper/copper plate interfaces was also measured to calibrate the ICR between the sample and carbon paper. The uncoated and ZrCN coated Ti−6Al−4V, after potentiostatic polarization in a
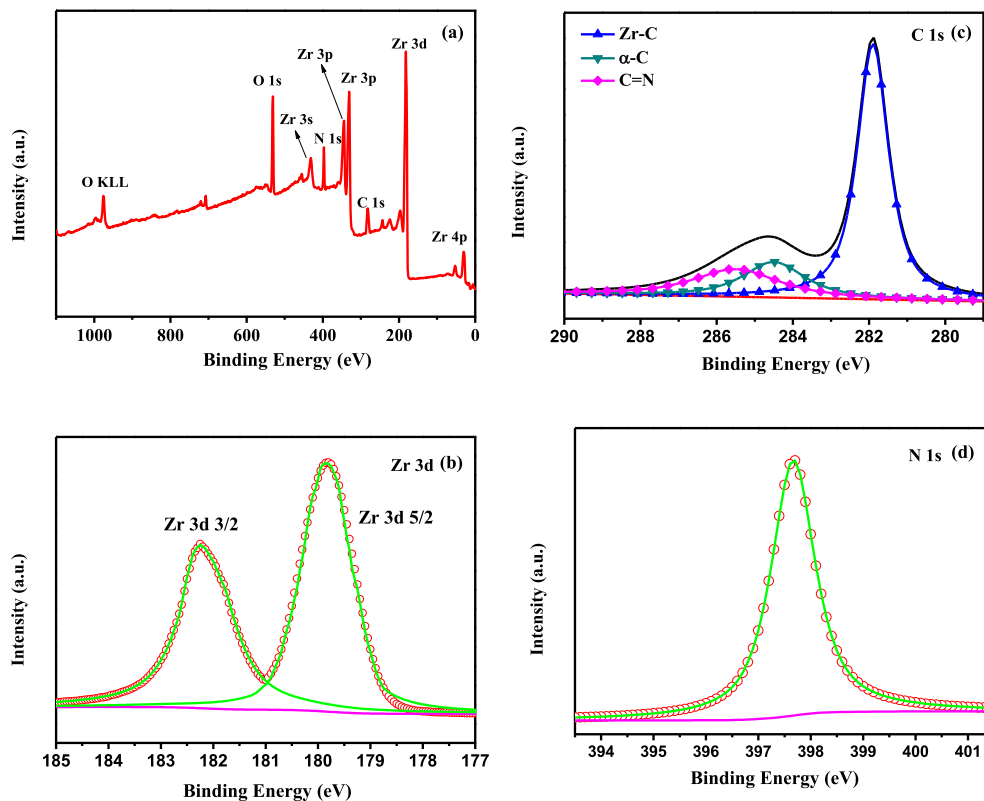

Fig. 2. (a) XPS survey spectra of the as-deposited ZrCN coating. The high-resolution XPS spectra for Zr 3d (b), C 1s (c) and N1s (d) peaks collected from the ZrCN coating.

simulated cathodic environment, were also investigated to understand the influence of any corrosion on ICR. The hydrophilicity of the sample surfaces was evaluated by contact angle analysis using the sessile drop method. An equal volume of distilled water was dropped carefully onto each sample by means of a micropipette. All measurements were made using a contact-angle meter (JC2000C,POWEREACH). Each measurement was repeated three times and then averaged.

3. Results and discussion

3.1. Phase analysis and nanoindentation testing

Fig. 1 displays the typical XRD pattern recorded from the ZrCN coating deposited onto a Ti-6A1-4V substrate. For comparison, the JCPDS cards No 35-0784 (cubic ZrC) and 35-0753 (cubic ZrN), are also presented (represented by vertical lines). It is clear that the recorded peaks of the coating are shifted slightly towards higher Bragg angles compared to the JCPDS values for ZrC, but towards lower Bragg angles compared to the JCPDS values for ZrN. This result indicates that the coating is distinctly characteristic of a mutual solid solution between ZrC and ZrN, due to the solid

solution effect through the direct substitution of carbon into the nitrogen lattice positions. Four diffraction peaks recorded from the coating arising from the (111), (200), (220) and (311) reflections for the NaCl type of crystalline structure were clearly identified. Further, the ZrCN (111) peak was noted to be relatively intense, indicating a strong preferred (111) crystallographic texture. In general, the presence of a highly ionized plasma, was considered to favor the film growth in the most densely packed [111] direction [22].

To further investigate the chemical composition and bonding states of the coating, XPS analysis was performed on the surface of the ZrCN coating after sputtering with a 3 keV Ar^+ ion beam for 600 s. In the XPS survey spectrum of the coating (Fig. 2(a)), the Zr 3d, C 1s and N 1s core level principal peaks were determined, as expected. According to the relative atomic concentration calculated from the Zr 3d, C 1s and N1s XPS peak areas, the elemental composition of the ZrCN coating in at.% was: Zr: 47.1, C: 22.4 and N: 30.5. On the basis of the Zr–C–N ternary phase diagram [23], the coating should lie within a two phase region containing both δ-$Zr(C_xN_{1-x})_{1-y}$ and either amorphous C or CN_x [24]. Fig. 2(b)–(d) shows the Zr 3d, C 1s and N 1s core level spectra of the ZrCN coating, respectively. Because of spin–orbit coupling, the Zr 3d core
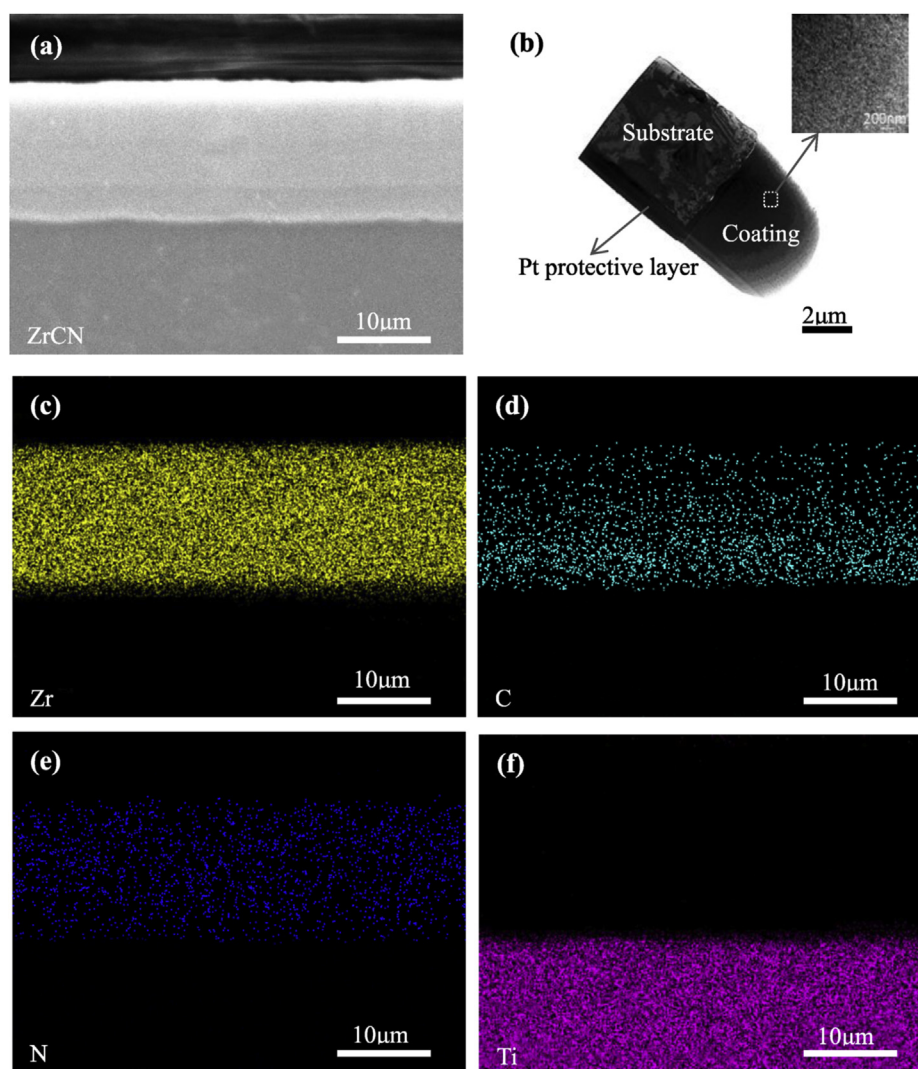

Fig. 3. (a) SEM cross-sectional image of the ZrCN coating; (b) A typical cross-sectional bright-field TEM image of the ZrCN coating and the corresponding EDS elemental mapping of Zr (c),C (d) and N(e) for the ZrCN coating.

level spectrum was reported to consist of both the Zr $3d_{3/2}$ and Zr $3d_{5/2}$ photoelectron lines with a theoretical ratio Zr $3d_{3/2}$/Zr $3d_{5/2}$ of 0.6 and a spine orbit splitting of 2.4 eV [25]. In the Zr 3d spectrum, the peak of Zr $3d_{5/2}$ is centered at 179.9 eV, lying between the binding energies of Zr $3d_{5/2}$ for ZrC (179.1 eV) and ZrN(180.6 eV), which is assigned to Zr–C–N bonds [26]. The C 1s spectrum is composed of a strong peak located at 282.1 eV, identified to represent Zr–C–N bonding [27] and a broad peak centered at 284.8 eV, which can be deconvoluted into two components, corresponding to an amorphous carbon (a-C) peak at 284.5 eV and C–N bond peak at 285.5 eV [28]. The N 1s spectrum exhibits only one peak at 397.7 eV, assigned to Zr–C–N bonding. Combining the XPS analysis with XRD results, it can be thus inferred that the coating consists of a mixture of crystalline Zr carbonitride together with amorphous C and CN_x phase.

The microstructure of the ZrCN coating is shown in the cross-sectional SEM and bright-field TEM micrographs shown in Fig. 3(a) and (b), respectively. It is evident that the coating with a thickness of about 15 μm exhibits a homogenous and dense structure, free of any visible pores or cavities across the entire coating thickness. The coating also appears to be well adhered to the substrate. The cross-sectional TEM images confirm that the coating exhibits a granular morphology, and no evidence of a columnar microstructure that is typical for coatings grown under low energetic ion bombardment and limited adatom mobility conditions [29]. For these coatings, a number of voids are evident between fiber-shaped columns derived from atomic shadowing and limited surface diffusion [30]. These voids may act as inward diffusion paths for corrosive species into the substrate, promoting galvanic corrosion between the coating and substrate [31]. From a corrosion prevention perspective, a dense structure provides better shielding effect to effectively retard aggressive ion ingress into the substrate material.

The fine-grained, dense microstructure of the ZrCN coating may be attributed to the following aspects. Firstly, a higher deposition temperature employed in this work, compared with other deposition techniques [32,33]. High deposition temperature enhances the mobility of atoms and provides impinging particles with more energy and is conducive to overcoming the self-shadowing effect exerted by previously deposited atoms, thereby reducing the density of defects. Secondly, the presence of an amorphous phase in this coating can interrupt columnar grain growth through stimulating continuous renucleation, as described by Barna [34]. Thirdly, the bombardment effect of the high-ionization plasma promotes the nucleation of nanocrystalline grains during the coating growth process [35]. Moreover, EDS mapping analysis (Fig. 3(c) − (f)) reveals that Zr, C and N elements are distributed uniformly across the coating.

Fig. 4 shows typical plan-view TEM bright-/dark-field images obtained from the ZrCN coating, together with the corresponding selected area diffraction (SAD) patterns. Clearly, the coating has a polycrystalline structure composed of equiaxed grains with an
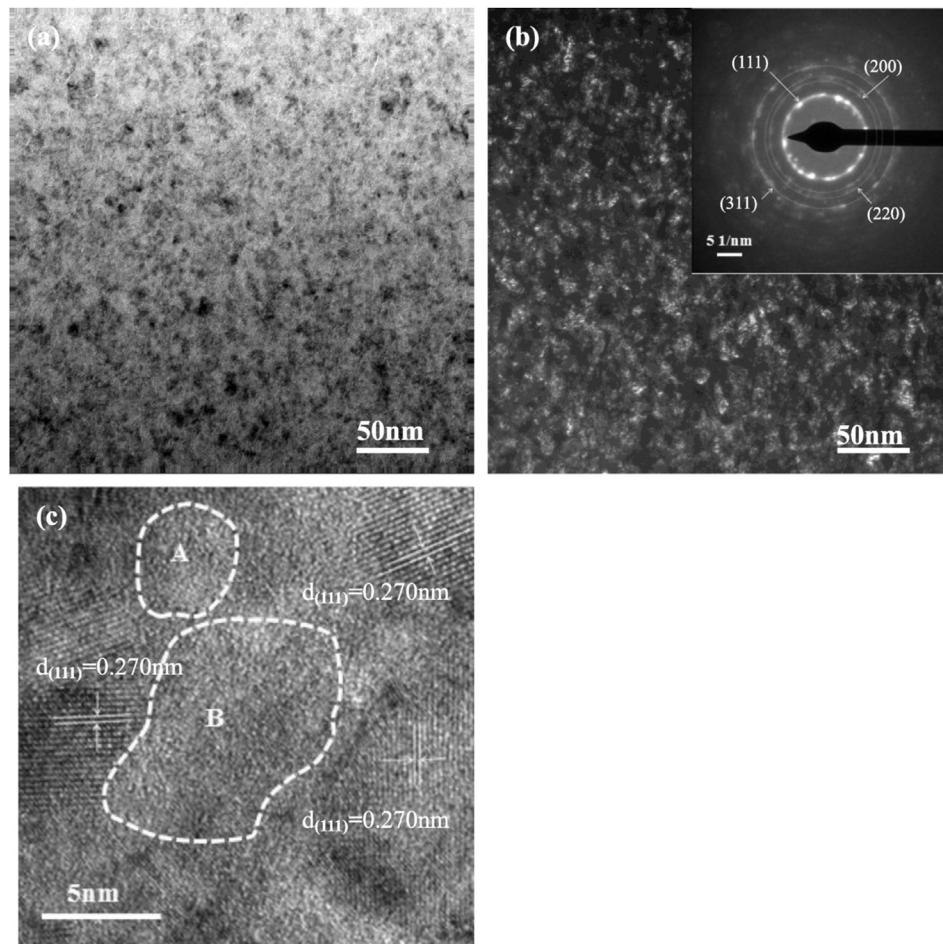

Fig. 4. Bright-field (a) and dark-field (b) TEM images of the ZrCN coating. The inset in Fig. 4(b) is a SAD pattern of ZrCN phase. A high-resolution electron microscopy (HRTEM) image of the as-deposited ZrCN coating(c) (amorphous region marked with A and B).

average diameter of about 10 nm, calculated from the dark-field image. The electron diffraction shows the characteristic diffraction rings consistent with the presence of face-centered cubic (fcc) B1−NaCl−structure, specifically, the first four rings corresponding to the (111), (200), (220) and (311) lattice planes. The higher intensity of the ZrCN (111) plane confirms further that the coating has a strong (111) preferred orientation, in agreement with the XRD results. A bright-field HRTEM lattice image (Fig. 4(c)) further confirms that the coating is characterized by a nanocomposite structure, in which individual ZrCN crystal grains, with (111) crystal plane more frequently observed. These grains appear to be embedded in the regions (marked with A and B), which exhibit an amorphous structure.

The representative load−displacement (p−h) curves obtained from nanoindentation tests for the ZrCN coating and uncoated Ti-6A1-4V are presented in Fig. 5. Under the same maximum load of 20 mN, the ZrCN coating shows less plastic deformation with a lower maximum indentation depth and residual depth as compared to uncoated Ti-6A1-4V. This indicates a greater resistance to local plastic deformation after coating with ZrCN. Note that the maximum indentation depth is smaller than 10% of the coating thickness, indicating that the contribution to the measured mechanical properties from the substrate is negligible. The hardness and elastic modulus of the ZrCN coating are determined to be 19.4 and 305.6 GPa, respectively, which is comparable to that of ZrCN coatings reported by other researchers [36].

The open circuit potentials (E_{OCP}) of the ZrCN coating and uncoated Ti-6A1-4V were recorded as a function of the immersion time over a period of 3600 s in 0.5 M H_2SO_4 solution with different concentrations of HF (namely, 2,4 and 6 ppm) at 70 °C, as shown in Fig. 6. As is well known, the value of E_{OCP} depends upon the experimental conditions, including the composition, temperature and oxygen content of electrolyte, and also on the surface state of the specimen [37]. As can be seen from Fig. 6, in the first moments of immersion, the E_{OCP} moves rapidly towards a more positive value, due to the initial formation and growth of a passive oxide film, followed by reaching a stationary value. With an increase in the concentrations of HF, the E_{OCP} shifts to more negative values and the time taken to reach a steady E_{OCP} is prolonged. This is because the increase of F⁻ ions and decrease of pH reduce the stability of the passive film. However, at any given concentration of HF, the ZrCN coating exhibits a more electropositive open circuit

potential than the uncoated Ti-6A1-4V and requires a shorter time to reach a stable value, revealing that the coating can more quickly form a more noble passive film in contrast to the uncoated substrate. According to the mixed potential theory, when two conductive phases are in electrical contact, the measured E_{OCP} is located between the E_{OCP} of both phases. Calderon et al. [38] suggested that the presence of an amorphous carbon phase enhanced the E_{OCP} of the ZrCN coating, because of its higher inertness compared with the pure ZrC_xN_{1-x} phase.

The potentiodynamic polarization curves for the ZrCN coating and uncoated Ti-6A1-4V in simulated anodic and cathodic PEMFC environments, presented in asemi-logarithmic scale, are shown in Fig. 7. Before each measurement the specimens were polarized cathodically for 10 min to provide more reproducible initial conditions for the specimen surface. As shown in Fig. 7(a) and (b), in both cases, the plots of the ZrCN coating display a marked shift towards the nobler direction and, simultaneously, downward displacement in the cathodic and anodic branches to a lower current region relative to that of uncoated Ti-6A1-4V. These shifts are related to the kinetic of the corrosion reactions, such as active anodic dissolution and reduction of hydrogen ions [39], signifying that the coating exhibits a lower electrochemical active behavior,
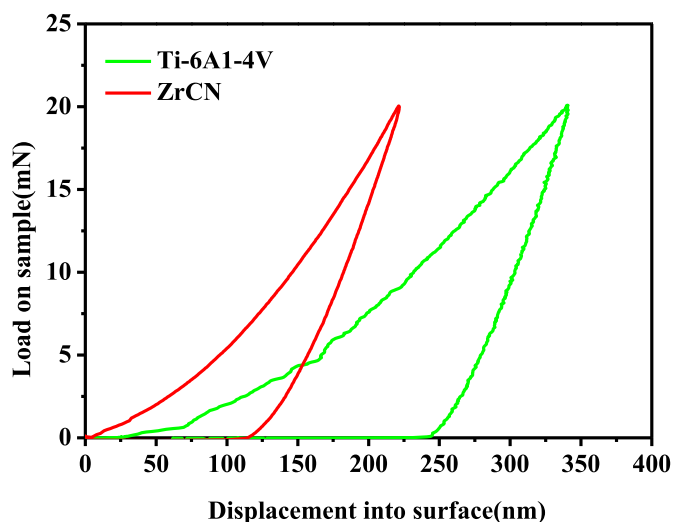

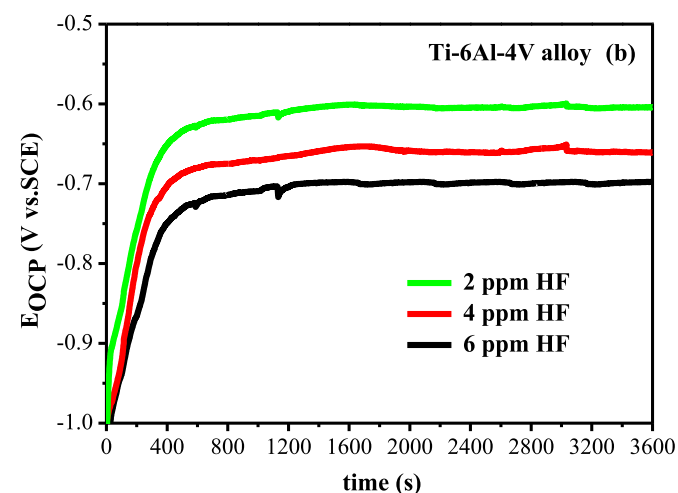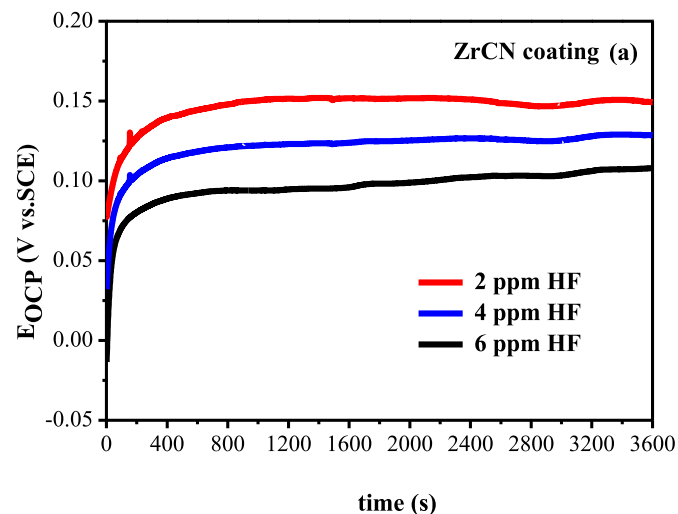Fig. 5. Load−displacement curves of the as-deposited ZrCN coating and bare Ti-6A1-4V alloy.

Fig. 6. The open circuit potential (E_{OCP}) values as a function of immersion time for (a) the as-deposited ZrCN coating and uncoated Ti-6A1-4V (b) in 0.5 M H_2SO_4 solution with different concentrations of HF (namely, 2,4 and 6 ppm) at 70 °C.
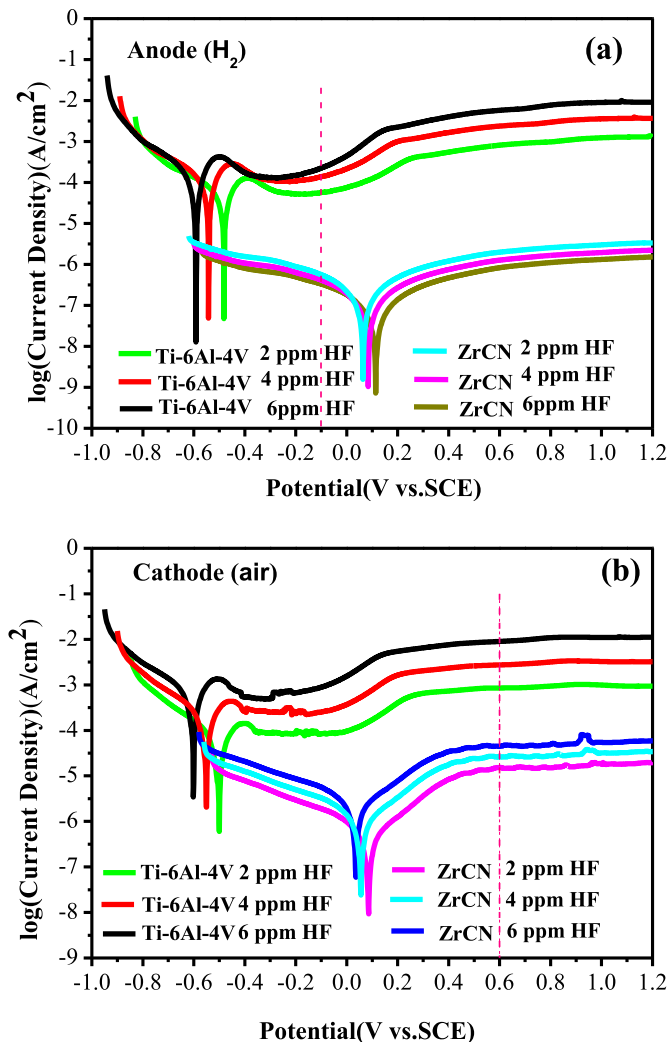
Fig. 7. The potentiodynamic polarization curves for the ZrCN coating and uncoated Ti-6A1-4V in simulated anodic (a) and cathodic (b) PEMFC environments.

behavior at more positive potentials. The values of the related electrochemical parameters, i.e., corrosion potential (E_{corr}), corrosion current density (i_{corr}), protective efficiency (P_e) of the coating and anodic (β_a) and cathodic (β_c) Tafel slopes derived from the polarization curves using Tafel analysis are summarized in Table 1. Moreover, the current densities at the operating potential in both the anodic and cathodic environments are also listed in Table 1. In general, the surface is more active, or less noble, if the E_{corr} is more negative (or less positive) and vice versa. The corrosion resistance is better if the i_{corr} at E_{corr} or the current densities under overpotential is lower. In both the anodic and cathodic environments, an increase in HF concentration accelerates the corrosion process, manifested by decreasing E_{corr} and increasing i_{corr}, which may be explained in terms of increasing the ionic strength of the medium by the addition of F^- and lower pH values. By comparing E_{corr} and i_{corr} data, it is found that the ZrCN coating has better corrosion resistance than uncoated Ti-6A1-4V. At the typical PEMFC cathodic operation potential of $+0.6$ V_{SCE}(Fig. 7b), with increasing HF concentration, the current densities of uncoated Ti−6Al−4V increase by an order of magnitude from 10^{-4} to 10^{-3} A cm^{-2}, which are 1−2 orders of magnitude larger than that for the ZrCN coating. This indicates that the ZrCN coating acts as an inhibitor of the corrosive solution's effect and can effectively retard the inward penetration of ions, such as H^+ and F^- ions present in the corrosive medium. Specifically, at the anodic operating potential of -0.1 V_{SCE}, the corrosion current densities of the uncoated Ti−6Al−4V are ~10^{-5} to10^{-4} A cm^{-2}, whereas, since the anodic operating potential is cathodic to the corrosion potential of the ZrCN coating, the ZrCN coating has negative current densities, thus being completely protected from corrosion attack in the anodic environment through cathodic protection.

Also, the protective efficiency (P_e) of the coating was determined from the polarization curves using the following equation [40]:

$$P_e = 100 \times \left(1 - i_{corr,\ coating}\Big/i^0_{corr,\ substrate}\right)$$

where $i_{corr,\ coatings}$ and $i_{corr,\ substrate}$ are the corrosion current densities of the coating and substrate, respectively. As shown in Table 1, the ZrCN coating shows a high protective efficiency of all above 98%, denoting that the coating can effectively protect the surface of the Ti−6Al−4V substrate from corrosion attack in an aggressive PEMFC operating environment.

In order to study the corrosion stability of the ZrCN coated Ti-6A1-4V under aggressive PEMFC working conditions, potentiostatic polarization tests were performed on the ZrCN coating and

inhibiting both the anodic and cathodic processes. Moreover, regardless of the concentration of HF, the coating is characterized by typical passive behavior with a wide passive plateau in the anodic domain, whereas uncoated Ti-6A1-4V is characterized by a very narrow passive region followed immediately by trans-passive

Table 1
Electrochemical parameters for the ZrCN coating and uncoated Ti−6Al−4V obtained from polarization curves.

| Samples	E_{corr} (V vs. SCE)	i_{corr} (μA cm^{-2})	β_a (V/decade)	$-\beta_c$ (V/decade)	0.6V/-0.1V (A·cm^{-2})	P_e
Cathode						
Ti−6Al−4V 2 ppm	−0.50	12.36	247.15	123.17	8.51×10^{-4}	−
Ti−6Al−4V 4 ppm	−0.55	44.53	223.45	119.76	2.75×10^{-3}	−
Ti−6Al−4V 6 ppm	−0.61	68.29	212.34	108.94	8.19×10^{-3}	−
ZrCN 2 ppm	0.09	1.24×10^{-1}	237.26	198.35	1.51×10^{-5}	98.9%
ZrCN 4 ppm	0.06	5.42×10^{-1}	219.82	182.46	2.63×10^{-5}	98.7%
ZrCN 6 ppm	0.04	9.85×10^{-1}	204.73	173.69	4.47×10^{-5}	98.6%
Anode						
Ti−6Al−4V 2 ppm	−0.48	8.03	258.53	132.21	5.75×10^{-5}	−
Ti−6Al−4V 4 ppm	−0.54	10.2	235.42	121.34	1.41×10^{-4}	−
Ti−6Al−4V 6 ppm	−0.59	11.0	221.13	118.45	2.19×10^{-4}	−
ZrCN 2 ppm	0.11	4.32×10^{-2}	241.25	204.34	-3.31×10^{-7}	99.5%
ZrCN 4 ppm	0.08	6.80×10^{-2}	225.63	197.65	-4.07×10^{-7}	99.3%
ZrCN 6 ppm	0.06	9.41×10^{-2}	208.47	179.58	-5.62×10^{-7}	99.1%
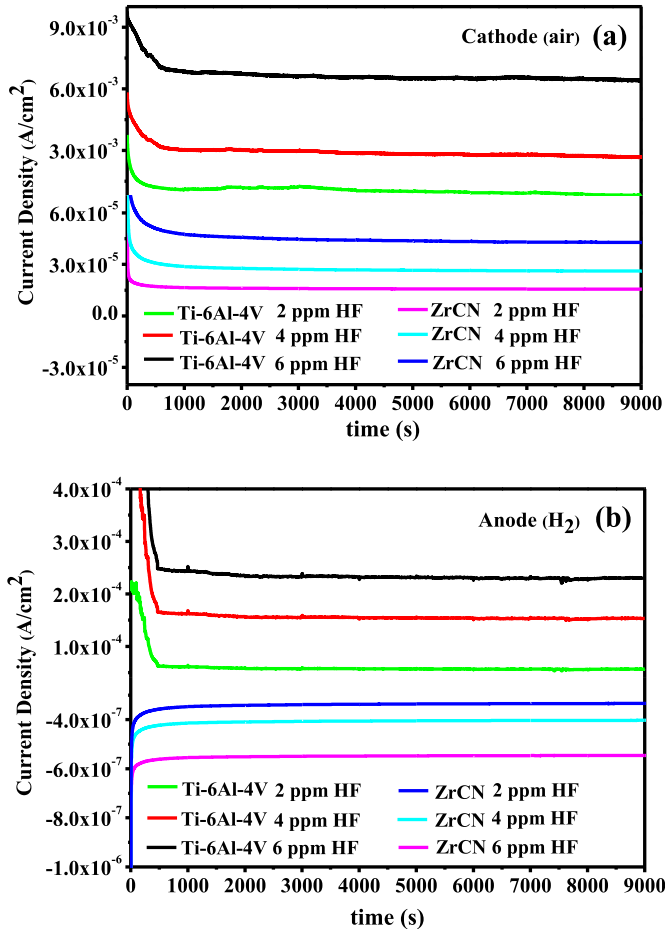
Fig. 8. Potentiostatic polarization curves of the ZrCN coating and the uncoated Ti-6Al-4V at cathode (+0.6 VSCE purged with air) (a) and anode (−0.1 VSCE purged with H2) (b) potentials.

Table 2
Electrochemical parameters for the ZrCN coating and uncoated Ti−6Al−4V obtained from Potentiostatic polarization.

Samples	Cathode current density	Anode current density
Ti−6Al−4V 2 ppm	9.81×10^{-4} A cm^{-2}	1.54×10^{-4} A cm^{-2}
Ti−6Al−4V 4 ppm	2.82×10^{-3} A cm^{-2}	2.31×10^{-4} A cm^{-2}
Ti−6Al−4V 6 ppm	6.53×10^{-3} A cm^{-2}	5.69×10^{-4} A cm^{-2}
ZrCN 2 ppm	1.57×10^{-5} A cm^{-2}	-3.36×10^{-7} A cm^{-2}
ZrCN 4 ppm	2.64×10^{-5} A cm^{-2}	-4.04×10^{-7} A cm^{-2}
ZrCN 6 ppm	4.35×10^{-5} A cm^{-2}	-5.47×10^{-7} A cm^{-2}

uncoated Ti-6Al-4V at anode and cathode potentials in a simulated PEMFC solution (anode environment: −0.1 V$_{SCE}$; cathode environment: +0.6 V$_{SCE}$), as shown in Fig. 8. The values of the related electrochemical parameters for the ZrCN coated Ti-6Al-4V and uncoated Ti-6Al-4V are summarized in Table 2. In the cathodic condition (Fig. 8(a)), the current densities recorded from the ZrCN coated and uncoated Ti-6Al-4V drop rapidly to the lower value at the initial stage of reaction due to the formation of a passive film and then exhibit constant values. With increasing HF concentration, the current densities of the uncoated Ti-6Al-4V increase by an order of magnitude from 10^{-4} to 10^{-3} Acm^{-2}, which was found to be 1−2 orders of magnitude higher than that for the ZrCN coating. As shown in Fig. 8(b), at an anodic potential of −0.1 V$_{SCE}$, the current densities of ZrCN coated Ti-6Al-4V is negative, regardless of the concentrations of HF, whereas the corrosion current densities of
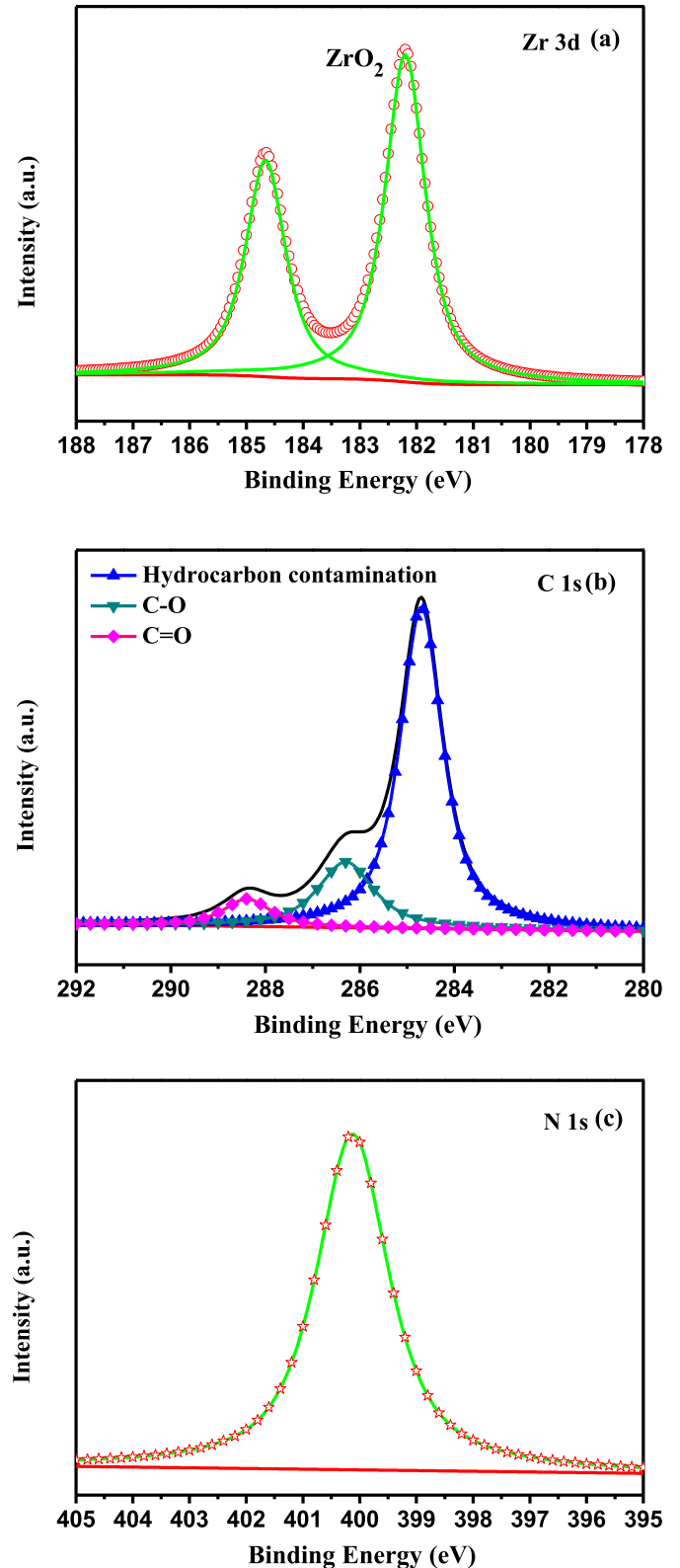

Fig. 9. The high-resolution XPS spectra for Zr 3d (a), C 1s (b) and N1s (c) peaks collected from passive film formed on the ZrCN coating after potentiostatic polarization at +0.6 V$_{SCE}$ purged with air for 2.5 h in a 0.5 M H$_2$SO$_4$ + 6 ppm HF solution.

the uncoated Ti-6Al-4V is positive, which is in accordance with the results obtained from the potentiodynamic polarization tests.

To investigate the constituent of the passive film formed on the

ZrCN coating, XPS analysis was conducted on the coating after potentiostatic polarization at +0.6 V_{SCE} purged with air for 2.5 h in a 0.5 M H_2SO_4 + 6 ppm HF solution. As shown in Fig. 9 (a), the Zr 3d spectrum consists of a doublet Zr $3d_{5/2}$ and Zr $3d_{3/2}$ peaks at 182.2 and 184.6 eV, corresponding to Zr–O bonds in ZrO_2. This value is 0.4 eV less than the binding energy of stoichiometric ZrO_2 [41], presumably arising from the formed ZrO_2 containing a small amount of carbon or nitrogen [42]. The C1s spectrum (Fig. 9(b)) can be deconvoluted into three components. The peaks located at 284.7, 286.3 and 288.4 eV, respectively, are attributed to surface hydrocarbon contamination and to oxidized C–O and C=O states [43]. The N 1s spectrum (Fig. 9(c)) appears as a single peak located at 399.9 eV, corresponding to N–H bonds in NH_3 [44].

In order to shed more light on the effect of concentrations of HF on the corrosion behavior of the ZrCN coating, the corroded surface morphologies of both the ZrCN coated and uncoated Ti-6A1-4V after potentiostatic testing in the simulated cathodic condition with additions of either 2 or 6 ppm HF to 0.5 M H_2SO_4 solution were examined by SEM, as shown in Fig. 10. It can be seen from Fig. 10 (a) and (b) that the uncoated Ti–Al–4V shows α + β two-phase structure, often exposed by metallographic etching, and some large and deep holes can be observed, accompanied by substantial evidence of material dissolution. Clearly, the bare Ti-6A1-4V surface has undergone strongly damage and the corrosion severity increases with the concentration of HF. H^+ and F^- ions present in the corrosion medium can penetrate the passive film formed on the bare Ti-6A1-4V, resulting in it being locally disrupted. Then, an active galvanic cell is formed between the anodic zone of the fresh metal underneath and the surrounding cathodic region comprising the rest of the surface that remains passive. The significant difference in surface area between the anode and the cathode gives rise to a high current density at the initiation site and, hence, accelerates the corrosion degradation of the material, causing the pits to penetrate deeper. An increase in H^+ and F^- ions concentration promotes the development of localized corrosion process and even causes a rupture of the outer passive film [45], which can explain

the high currents produced during the potentiostatic tests on the bare Ti-6A1-4V. In contrast, as shown in Fig. 10(c) and (d), the corroded surface of the ZrCN coated Ti-6A1-4V has a smooth and compact appearance with no evidence of pitting, suggesting that the passive films grown on the ZrCN coating are more robust and offer better corrosion resistance in a 0.5 M H_2SO_4 solution containing different HF concentrations.

To obtain more information about the mechanisms of corrosion of the ZrCN coating, electrochemical impedance spectroscopy, EIS, measurements were performed in 0.5 M H_2SO_4 solution containing different HF concentrations at 70 °C. Fig. 11 shows the representative Nyquist and Bode plots for the ZrCN coated and uncoated Ti-6A1-4V obtained from the impedance data measured at their respective E_{OCP}, after steady state potential was attained. From Fig. 11(a) and (c), both of the Nyquist plots have a depressed semicircular shape across the entire frequency range and the major difference between the two samples is that size of the spectrum obtained from the ZrCN coating is distinct from the uncoated Ti-6A1-4V. With increasing concentration of HF, the semicircles of the two samples decrease significantly in diameter, whereas the diameter of semicircles for the ZrCN coating are much greater than that for uncoated Ti-6A1-4V. From the corresponding Bode magnitude plots shown in Fig. 11(b) and (d), the log |Z| versus log f of the two samples are linear with a slope close to −1. Although the frequency range of the linear region for the two samples decreases with an increase in HF concentration, the ZrCN coating is linear over a broader frequency range compared with the uncoated Ti-6A1-4V at a given HF concentration, indicating that the passive layer formed on the ZrCN coating is more protective than that on the uncoated Ti-6A1-4V. Furthermore, the change trends of the values of low-frequency limit ($|Z|_{f \to 0}$) with an increase of HF concentration are also almost the same as that of the frequency range of the linear region for the two samples. From the Bode phase plots, at a given HF addition, the ZrCN coating exhibits a plateau with a maximum phase angle near −90° in the middle and low frequency range, which is broader than that of the uncoated Ti-
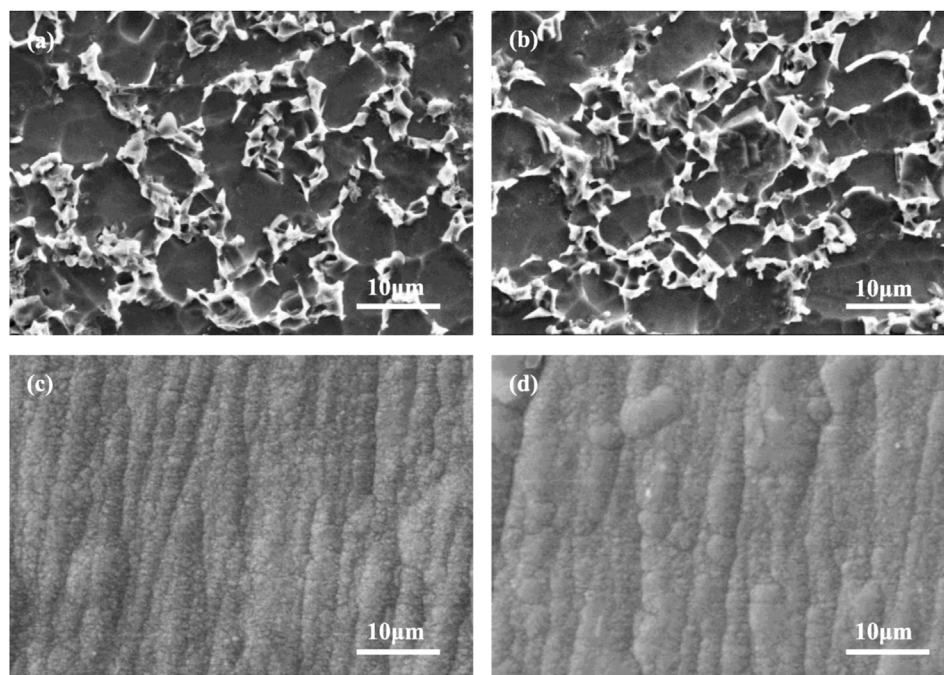

Fig. 10. The corroded surface morphologies of bare Ti-6A1-4V ((a) and (b)) and the ZrCN coating ((c) and (d)) after potentiostatic testing in the simulated cathodic condition with addition of 2 and 6 ppm HF to 0.5 M H_2SO_4 solution. (a) and (c):2 ppm HF; (b) and (d):6 ppm HF.
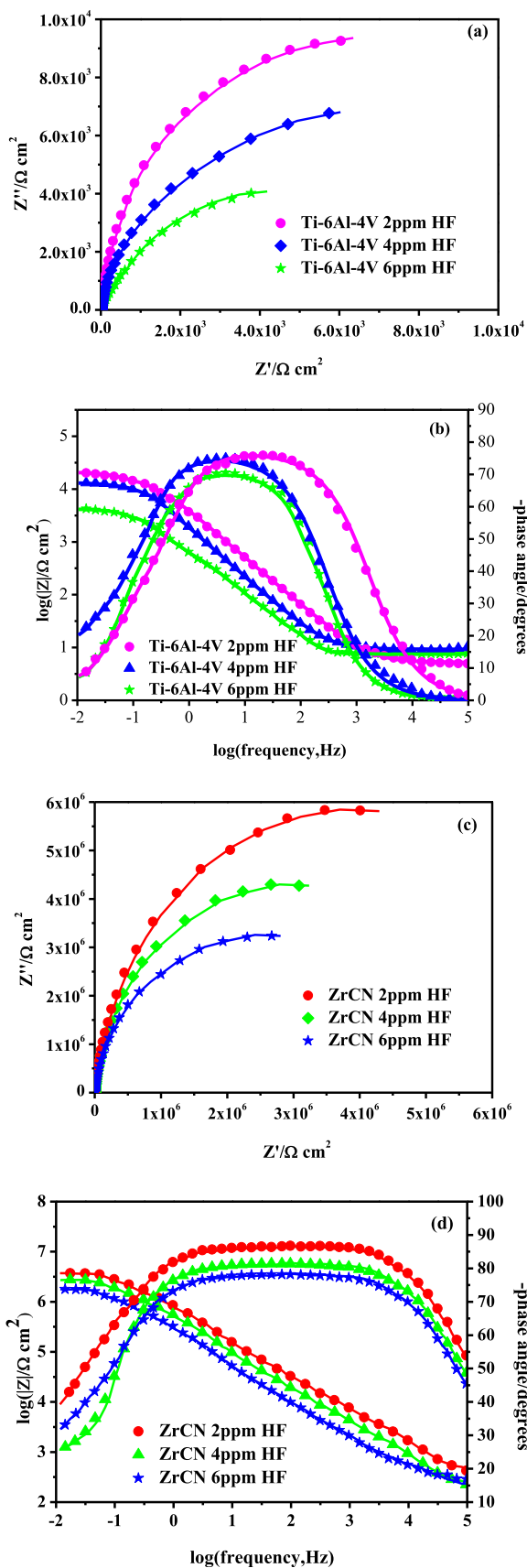
Fig. 11. The representative Nyquist and Bode plots for uncoated and the ZrCN coated Ti–6Al–4V at their respective E_{OCP} in 0.5 M H_2SO_4 solution containing different HF concentrations at 70 °C. The bare Ti–6Al–4V: (a) Nyquist plot, (b) Bode plot; the ZrCN coating: (c) Nyquist plot, (d) Bode plot.

6A1-4V, suggesting that the ZrCN coating is more capacitive and leads to lower penetration of the electrolyte as compared to the uncoated Ti-6A1-4V.

The measured impedance data are analyzed using various equivalent circuits (ECs) comprising an assembly of electrical circuit elements that reflect the electrochemical process responsible for the two samples. Only one time constant was observed in the Bode plots (Fig. 11(b)) over the frequency range between 100 kHz and 10 mHz present and the experimental impedance data obtained from the uncoated Ti-6A1-4V can be modeled by one time constant equivalent circuit $R_s(R_pQ_p)$ (Fig. 12(a)), where R_s and R_p are the solution and the parallel (passive film) resistances, respectively, and Q is constant phase element (CPE), which takes into account the capacitive behavior of the film. This equivalent circuit has been generally used to fit oxides grown on Ti alloys under different environments [46,47]. In the case of the ZrCN coating, the broad plateau in the Bode phase plots may originate from two overlapped time constants corresponding to two merging phase maximum in the medium frequency (MF) and low frequencies (LF) regions. Based on this analysis, the two R–Q elements equivalent circuit $(Rs(Q_{dl}(R_{ct}(Q_bR_b))))$ was adopted to fit the experimental impedance data of the ZrCN coating, as shown in Fig. 12(b). In this circuit, the high frequency time constant associates to the double layer capacitance (C_{dl}) and the charge transfer resistance (R_{ct}) of the electrochemical process at the passive layer or/solution interface, while the low frequency time constant (Q_bR_b) is related to the passive layer. It can be seen from Table 3 that simulated results (shown as individual points) match the experimental data (shown as solid lines) well with the chi-squared (χ^2) values being of the order of $10^{-3} \sim 10^{-4}$, signifying that the two proposed EEC reasonably reflect the actual electrochemical process occurring on the test samples in the simulated PEMFC environments. Table 3 compiles the numerical values of circuit elements from the fitting procedure. As can be seen from Table 3, for the ZrCN coating, the resistance of the passive film (R_b) is two orders of magnitude larger than the charge transfer resistance (R_{ct}), suggesting that the contribution of the resistance of the passive layer to the overall corrosion resistance is predominant, i.e., the resistance to ionic transport should depend primarily on the passive film, rather than the passive film–solution interface. With increasing concentration of HF, the resistance of the passive film (R_b) decreased slightly, being of the order of magnitude of $\sim 10^7$ Ω cm^2, which, however, is an improvement by four orders of magnitude compared to uncoated Ti-6A1-4V. In addition, the time constant (τ), expressed as $\tau = R \times C$, can be directly used to evaluate the rate of the relevant electrochemical process, including the ionic migration within the oxide film and charge transfer [48]. When one takes the reciprocal of the obtained product values, the rate of relevant electrochemical process is determined. Apparently, the values of τ for the two samples decrease with increasing HF concentration, denoting an increased corrosion rate. At any given concentration of HF, the values of $\tau 2$ for the ZrCN coating are significantly larger than that of bare Ti-6A1-4V, denoting that the ZrCN coating provides a more effective barrier to corrosive attack and thus retards electrochemical corrosion process.

The interfacial contact resistance between the bipolar plates and the gas diffusion layer (GDL) is one of the most important resistances that occur at all interfaces inside a PEMFC stack, which overall is a critical factor affecting cell performance in fuel cell applications [49]. The high electrical conductivity of the bipolar plates is favorable for minimizing the loss of power obtained from the PEMFC stack and maximizing PEMFC stack efficiency [50]. Fig. 13 displays the interfacial contact resistance (ICR) as a function of compaction force from 20 to 260 N cm^{-2} for the ZrCN coated Ti-6A1-4V before and after 2.5 h potentiostatic polarization at a cathode potential of $+0.6$ V_{SCE} in 0.5M H_2SO_4 + 6 ppm HF solution
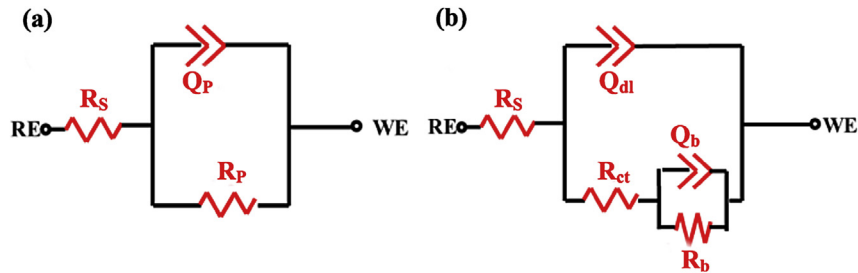
(a) **(b)**

Fig. 12. Equivalent electrical circuits used for modeling experimental EIS data of the bare Ti−6Al−4V (a) and ZrCN coating (b).

Table 3
Electrochemical parameters obtained from equivalent circuits simulation.

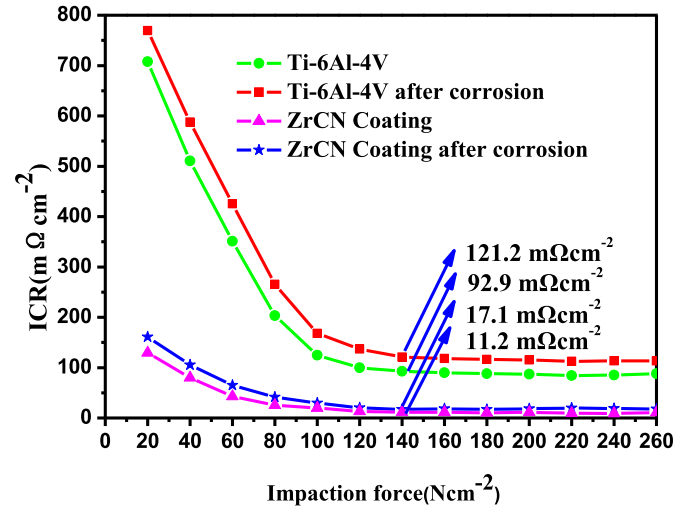|	Parameters	Ti−6Al−4V
0.5MH$_2$SO$_4$+2ppmHF	R$_s$ (Ω cm^2)	11.43 ± 0.01
	Q$_P$ (Ω^{-1} cm^{-2} s^n)	(3.47 ± 0.01) × 10^{-5}
	R$_P$ (Ω cm^2)	(5.52 ± 0.04) × 10^3
	C$_P$ (μF cm^{-2})	14.53
	τ$_p$ (s)	0.08
	χ^2	3.47 × 10^{-3}
0.5MH$_2$SO$_4$+4ppmHF	R$_s$ (Ω cm^2)	10.56 ± 0.02
	Q$_P$ (Ω^{-1} cm^{-2} s^n)	(5.62 ± 0.01) × 10^{-5}
	R$_P$ (Ω cm^2)	(2.41 ± 0.03) × 10^3
	C$_P$ (μF cm^{-2})	15.12
	τ$_p$ (s)	0.04
	χ^2	5.21 × 10^{-3}
0.5MH$_2$SO$_4$+6ppmHF	R$_s$ (Ω cm^2)	9.32 ± 0.01
	Q$_P$ (Ω^{-1} cm^{-2} s^n)	(6.67 ± 0.02) × 10^{-5}
	R$_P$ (Ω cm^2)	(1.03 ± 0.02) × 10^3
	C$_P$ (μF cm^{-2})	16.34
	τ$_p$ (s)	0.02
	χ^2	4.42 × 10^{-3}
	Parameters	ZrCN
0.5MH$_2$SO$_4$+2ppmHF	R$_s$ (Ω cm^2)	14.37 ± 0.02
	Q$_{dl}$ (Ω^{-1} cm^{-2} s^n)	(1.30 ± 0.02) × 10^{-6}
	R$_{ct}$ (Ω cm^2)	(9.34 ± 0.01) × 10^5
	C$_{dl}$ (μF cm^{-2})	1.16
	τ$_1$ (s)	1.08
	Q$_b$ (Ω^{-1} cm^{-2} s^n)	(4.23 ± 0.01) × 10^{-7}
	R$_b$ (Ω cm^2)	(9.65 ± 0.03) × 10^7
	C$_b$ (μF cm^{-2})	0.11
	τ$_2$ (s)	10.61
	χ^2	1.36 × 10^{-3}
0.5MH$_2$SO$_4$+4ppmHF	R$_s$ (Ω cm^2)	13.21 ± 0.01
	Q$_{dl}$ (Ω^{-1} cm^{-2} s^n)	(3.54 ± 0.03) × 10^{-6}
	R$_{ct}$ (Ω cm^2)	(4.12 ± 0.02) × 10^5
	C$_{dl}$ (μF cm^{-2})	2.09
	τ$_1$ (s)	0.86
	Q$_b$ (Ω^{-1} cm^{-2} s^n)	(8.46 ± 0.02) × 10^{-7}
	R$_b$ (Ω cm^2)	(3.02 ± 0.02) × 10^7
	C$_b$ (μF cm^{-2})	0.31
	τ$_2$ (s)	9.36
	χ^2	7.43 × 10^{-4}
0.5MH$_2$SO$_4$+6ppmHF	R$_s$ (Ω cm^2)	11.85 ± 0.02
	Q$_{dl}$ (Ω^{-1} cm^{-2} s^n)	(6.21 ± 0.02) × 10^{-6}
	R$_{ct}$ (Ω cm^2)	(2.28 ± 0.01) × 10^5
	C$_{dl}$ (μF cm^{-2})	3.38
	τ$_1$ (s)	0.77
	Q$_b$ (Ω^{-1} cm^{-2} s^n)	(9.75 ± 0.02) × 10^{-7}
	R$_b$ (Ω cm^2)	(1.63 ± 0.01) × 10^7
	C$_b$ (μF cm^{-2})	0.41
	τ$_2$ (s)	6.68
	χ^2	6.13 × 10^{-4}

Fig. 13. The interfacial contact resistance (ICR) as a function of compaction force from 20 to 260 N cm^{-2} for the ZrCN coated Ti-6A1-4V before and after 2.5 h potentiostatic polarization at a cathode potential of +0.6 V$_{SCE}$ in 0.5 M H$_2$SO$_4$ + 6 ppm HF solution open to air at 70 °C.

bare Ti-6A1-4V. The ICR decreases rapidly at relatively low compaction forces ranging from 20 to 120 N cm^{-2}. However, with further increases in the compaction force, the ICR values remain largely unchanged. Generally, contact resistance is determined by material properties, surface morphology, assembly pressure and operation conditions. The initial decrease in ICR can be attributed to an enhancement in the actual conductive area between the samples and carbon paper induced by increasing compaction force; however, above a certain value of compaction force, the effective contact area does not increase any further, and the nature of the sample surface and composition become the predominant factors that control ICR values [51]. Over the entire applied compaction force range, the ICR values of the ZrCN coated Ti-6A1-4V are much less than that of the uncoated sample at the same compaction force. At a compaction force of 140 N cm^{-2}, a typical compaction force of a single cell, for bare Ti−6Al−4V, a marked increase of ICR value from 92.9 mΩ cm^{-2} to 121.2 mΩ cm^{-2} is observed after potentiostatic polarization. This behavior can be attributed to the fact that the oxide film on the bare Ti−6Al−4V becomes thicker under a high cathode potential in an oxidizing atmosphere, further increasing electrical resistance. In the case of the ZrCN coated Ti-6A1-4V, no perceptible difference in the ICR value was observed before and after corrosion, and the ICR values only slightly increase from 11.2 to 17.1 mΩ cm^{-2}. The ICR values of the ZrCN coated Ti-6A1-4V are only slightly higher than the US DOE 2015 target of 10 mΩ cm^{-2}, but are comparable with that for plasma-nitrided layer and Cr electroplating coatings [52]. In fact, oxides can exhibit conductor, semiconductor or insulator features simply through varying their

open to air at 70 °C. For comparative purposes, the ICR of bare Ti-6A1-4V measured under the same condition is also plotted in Fig. 13. It can be observed that either before or after potentiostatic polarization for 2 h, the variation of the ICR of the ZrCN coated Ti-6A1-4V with compaction force has the similar behavior to that of
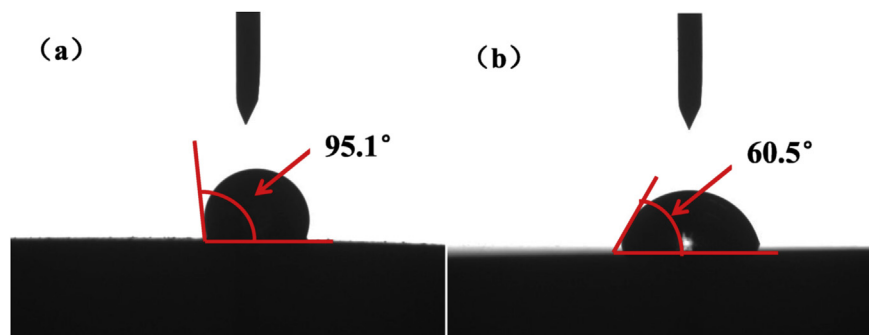
Fig. 14. The photographs of water droplet on the ZrCN coating (a) and the bare Ti–6Al–4V alloy (b).

stoichiometric compositions or by elemental doping. Based on the XPS results, carbon and nitrogen atoms incorporated into the ZrO$_2$ lattice may act as dopants, which may help improve surface conductivity and reduce the ICR value.

The presence of water in a PEMFC stack originates either from an oxygen reduction reaction at the catalyst cathode or is fed externally into the cell through humidification or the presence of cooling gases [53]. Moreover, excess water can not only block the reaction sites of neighboring electrodes, preventing the access of reactant gases to the cell, but also can accelerate the corrosion rate of the metallic bipolar plates [54]. To avoid issues associated with flooding and power degradation, due to the submergence of the catalyst, the surface wettability of the bipolar plate materials should be sufficiently low to immediately remove any redundant water from the PEMFC stack. Contact angle measurements provide a means to estimate the wettability of a surface [55]. A high contact angle denotes a low surface wettability. Fig. 14 shows photographs of water droplets formed on the ZrCN coated and bare Ti–6Al–4V. The average contact angle with water for the ZrCN coated Ti–6Al–4V is 95.1°, while that of bare Ti–6Al–4V is 60.5°. These results imply that the ZrCN coated Ti–6Al–4V alloy is much more hydrophobic than bare Ti–6Al–4V. Therefore, the ZrCN coating provides greater protection from accumulated water flooding the electrode system [3]. Furthermore, a lower wettability also means a lower fraction of the coated area is in contact with the electrolyte solution, thus lowering the extent of any corrosion that may occur.

4. Conclusions

A dense and uniform nanocrystalline ZrCN coating was deposited on to a Ti–6Al–4V substrate using a double glow discharge plasma technique. The coating with a thickness of about 15 μm exhibited a nanocomposite structure, in which equiaxed ZrCN grains, with an average value of about 10 nm, are separated by an amorphous C or CN$_x$ phase. The electrochemical behavior, electrical conductivity and surface wettability of the ZrCN coated Ti–6Al–4V were evaluated to assess its potential applicability as a PEMFC bipolar plate material. By comparing E_{corr} and i_{corr} data, it is found that the ZrCN coating has better corrosion resistance than the uncoated Ti-6A1-4V. The ZrCN coating has negative corrosion current densities at the anode operation potential of PEMFC (-0.1 V$_{SCE}$), providing cathodic protection for the Ti-6A1-4V substrate, while the current densities for the ZrCN coating is found to be 1–2 orders of magnitude lower than that for uncoated Ti-6A1-4V at a cathodic operation potential of $+0.6$ V$_{SCE}$. The results of EIS measurements showed that with increasing the concentration of HF, the resistance of the passive film (R_b) formed on the ZrCN coating decreased slightly, being of the order of magnitude of ~10^7 Ω cm^2, which is four orders of magnitude higher than that of uncoated Ti-6A1-4V.

At a compaction force of 140 Ncm^{-2}, the ICR values for the ZrCN coating were much lower than that of bare Ti-6A1-4V before and after potentiostatic polarization for 120 min. Moreover, the ZrCN coating is more hydrophobic than uncoated Ti-6A1-4V, which prevented accumulated water from flooding the electrode system and mitigated the extent of corrosive damage. Therefore, the ZrCN coated Ti–6Al–4V has great potential to be used as the candidate bipolar plate for PEMFC.

References

[1] S.R. Dhakate, S.S.R.B. Mathur, A Low-density graphite-polymer composite as a bipolar plate for proton exchange membrane fuel cells, Carbon Lett. 14 (1) (2013) 40–44.
[2] J.J. Hwang, W.R. Chang, F.B. Weng, et al., Development of a small vehicular PEM fuel cell system, Int. J. Hydrogen Energy 33 (14) (2008) 3801–3807.
[3] H. Tawfik, Y. Hung, D. Mahajan, Metal bipolar plates for PEM fuel cell—a review, J. Power Sources 163 (2) (2007) 755–767.
[4] A. Shanian, O. Savadogo, A non-compensatory compromised solution for material selection of bipolar plates for polymer electrolyte membrane fuel cell (PEMFC) using ELECTRE IV, Electrochimica Acta 51 (25) (2006) 5307–5315.
[5] M. Kumagai, S.T. Myung, S. Kuwata, et al., Application of Ni-free high nitrogen stainless steel for bipolar plates of proton exchange membrane fuel cells, Electrochimica Acta 54 (3) (2009) 1127–1133.
[6] S.R. Dhakate, S. Sharma, M. Borah, et al., Expanded graphite-based electrically conductive composites as bipolar plate for PEM fuel cell, Int. J. hydrogen energy 33 (23) (2008) 7146–7152.
[7] S.J. Lee, C.H. Huang, Y.P. Chen, et al., chemical treatment method for the aluminum bipolar plates of PEM fuel cells, J. Fuel Cell Sci. Technol. 2 (3) (2005) 208–212.
[8] J.R. Mawdsley, J.D. Carter, X. Wang, et al., Composite-coated aluminum bipolar plates for PEM fuel cells, J. Power Sources 231 (2013) 106–112.
[9] K.H. Hou, C.H. Lin, M.D. Ger, et al., Analysis of the characterization of water produced from proton exchange membrane fuel cell (PEMFC) under different operating thermal conditions, Int. J. hydrogen energy 37 (4) (2012) 3890–3896.
[10] H. Wang, J.A. Turner, Reviewing metallic PEMFC bipolar plates, Fuel Cells 10 (4) (2010) 510–519.
[11] S.H. Wang, J. Peng, W.B. Lui, et al., Performance of the gold-plated titanium bipolar plates for the light weight PEM fuel cells, J. Power Sources 162 (1) (2006) 486–491.
[12] Y. Show, M. Miki, T. Nakamura, Increased in output power from fuel cell used metal bipolar plate coated with aC film, Diam. Relat. Mater. 16 (4) (2007) 1159–1161.
[13] K. Feng, D.T.K. Kwok, D. Liu, et al., Nitrogen plasma-implanted titanium as bipolar plates in polymer electrolyte membrane fuel cells, J. Power Sources 195 (19) (2010) 6798–6804.
[14] S.H. Wang, J. Peng, W.B. Lui, Surface modification and development of titanium bipolar plates for PEM fuel cells, J. power sources 160 (1) (2006) 485–489.
[15] J.D. Gu, P.L. Chen, Investigation of the corrosion resistance of ZrCN hard

coatings fabricated by advanced controlled arc plasma deposition, Surf. Coat. Technol. 200 (10) (2006) 3341–3346.

[16] S.H. Yao, Y.L. Su, W.H. Kao, et al., Wear behavior of DC unbalanced magnetron sputter deposited ZrCN films, Mater. Lett. 59 (26) (2005) 3230–3233.

[17] C.M. Cotrut, V. Braic, M. Balaceanu, et al., Corrosion resistance, mechanical properties and biocompatibility of Hf-containing ZrCN coatings, Thin Solid Films 538 (2013) 48–55.

[18] S. Lædre, O.E. Kongstein, A. Oedegaard, et al., The effect of pH and halides on the corrosion process of stainless steel bipolar plates for proton exchange membrane fuel cells, Int. J. Hydrogen Energy 37 (23) (2012) 18537–18546.

[19] J. Xu, D.H. Lai, Z.H. Xie, et al., A critical role for Al in regulating the corrosion resistance of nanocrystalline Mo (Si$_{1-x}$ Al$_x$) 2 films, J. Mater. Chem. 22 (6) (2012) 2596–2606.

[20] W.C. Oliver, G.M. Pharr, An improved technique for determining hardness and elastic modulus using load and displacement sensing indentation experiments, J. Mater. Res. 7 (06) (1992) 1564–1583.

[21] J. Xu, S. Xu, P. Munroe, et al., A ZrN nanocrystalline coating for polymer electrolyte membrane fuel cell metallic bipolar plates prepared by reactive sputter deposition, RSC Adv. 5 (82) (2015) 67348–67356.

[22] D.C. Kothari, A.N. Kale, Recent trends in surface engineering using cathodic arc technique, Surf. Coat. Technol. 158 (2002) 174–179.

[23] J.M. Antunes, A. Cavaleiro, L.F. Menezes, et al., Ultra-microhardness testing procedure with Vickers indenter, Surf. Coat. Technol. 149 (1) (2002) 27–35.

[24] E. Silva, M.R. de Figueiredo, R. Franz, et al., Structure–property relations in ZrCN coatings for tribological applications, Surf. Coat. Technol. 205 (7) (2010) 2134–2141.

[25] M. Matsuoka, S. Isotani, W. Sucasaire, et al., X-ray photoelectron spectroscopy analysis of zirconium nitride-like films prepared on Si (100) substrates by ion beam assisted deposition, Surf. Coat. Technol. 202 (13) (2008) 3129–3135.

[26] F. Zhou, K. Fu, B. Liao, et al., Effect of carbon content on nanostructural, mechanical and electrochemical characteristics of self-organized nc-ZrCN/a-CN$_x$ nanocomposite films, Appl. Surf. Sci. 327 (2015) 350–357.

[27] C.H. Lai, Y.Y. Chang, H.L. Huang, et al., Characterization and antibacterial performance of ZrCN/amorphous carbon coatings deposited on titanium implants, Thin Solid Films 520 (5) (2011) 1525–1531.

[28] W. Yu, G.B. Ren, S.F. Wang, et al., Effect of gas pressure on the synthesis of carbon nitride films during plasma-enhanced chemical vapor deposition, Thin Solid Films 402 (1) (2002) 55–59.

[29] S. Carvalho, E. Ribeiro, L. Rebouta, et al., Effects of the morphology and structure on the elastic behavior of (Ti, Si, Al) N nanocomposites, Surf. Coat. Technol. 174 (2003) 984–991.

[30] J.A. Thornton, High rate thick film growth, Annu. Rev. Mater. Sci. 7 (1) (1977) 239–260.

[31] S. Myers, J. Lin, R.M. Souza, et al., The β to α phase transition of tantalum coatings deposited by modulated pulsed power magnetron sputtering, Surf. Coat. Technol. 214 (2013) 38–45.

[32] J. Vlček, J. Rezek, J. Houška, et al., Process stabilization and a significant enhancement of the deposition rate in reactive high-power impulse magnetron sputtering of ZrO 2 and Ta 2 O 5 films, Surf. Coat. Technol. 236 (2013) 550–556.

[33] E. Atanassova, P. Lytvyn, S.N. Dub, et al., Nanomechanical properties of pure and doped Ta2O5 and the effect of microwave irradiation, J. Phys. D Appl. Phys. 45 (47) (2012) 475304.

[34] P.B. Barna, M. Adamik, Fundamental structure forming phenomena of polycrystalline films and the structure zone models, Thin Solid Films 317 (1) (1998) 27–33.

[35] K. Macák, V. Kouznetsov, J. Schneider, et al., Ionized sputter deposition using

an extremely high plasma density pulsed magnetron discharge, J. Vac. Sci. Technol. A 18 (4) (2000) 1533–1537.

[36] C.S. Chen, C.P. Liu, Diffusion barrier properties of amorphous ZrCN films for copper metallization, J. Non cryst. solids 351 (49) (2005) 3725–3729.

[37] L. Reclaru, P.Y. Eschler, R. Lerf, et al., Electrochemical corrosion and metal ion release from Co-Cr-Mo prosthesis with titanium plasma spray coating, Biomaterials 26 (23) (2005) 4747–4756.

[38] S. Calderon, J.C. Oliveira, M. Evaristo, et al., Prediction of optimized composition for enhanced mechanical and electrochemical response of Zr-CN-Ag coatings for medical devices, Appl. Surf. Sci. 320 (2014) 570–580.

[39] J. Xu, Z.Y. Li, S. Xu, et al., A nanocrystalline zirconium carbide coating as a functional corrosion-resistant barrier for polymer electrolyte membrane fuel cell application, J. Power Sources 297 (2015) 359–369.

[40] K. Nozawa, K. Aramaki, One-and two-dimensional polymer films of modified alkanethiol monolayers for preventing iron from corrosion, Corros. Sci. 41 (1) (1999) 57–73.

[41] C. Monticelli, F. Zucchi, A. Pagnoni, et al., Corrosion of a zirconium diboride/ silicon carbide composite in aqueous solutions, Electrochimica acta 50 (16) (2005) 3461–3469.

[42] V. Craciun, E.J. McCumiskey, M. Hanna, et al., Very hard ZrC thin films grown by pulsed laser deposition, J. Eur. Ceram. Soc. 33 (12) (2013) 2223–2226.

[43] G. Beamson, D. Briggs, High Resolution XPS of Organic Polymers, Wiley, 1992.

[44] J. Xu, L. Liu, P. Munroe, et al., The nature and role of passive films in controlling the corrosion resistance of MoSi 2-based nanocomposite coatings, J. Mater. Chem. A 1 (35) (2013) 10281–10291.

[45] S.K. Mukherjee, P.K. Barhai, S. Srikanth, Comparative evaluation of corrosion behaviour of type K thin film thermocouple and its bulk counterpart, Corros. Sci. 53 (9) (2011) 2881–2893.

[46] M. Metikoš-Huković, A. Kwokal, J. Piljac, The influence of niobium and vanadium on passivity of titanium-based implants in physiological solution, Biomaterials 24 (21) (2003) 3765–3775.

[47] A.K. Shukla, R. Balasubramaniam, Effect of surface treatment on electrochemical behavior of CP Ti, Ti–6Al–4V and Ti–13Nb–13Zr alloys in simulated human body fluid, Corros. Sci. 48 (7) (2006) 1696–1720.

[48] A. Arutunow, K. Darowicki, DEIS assessment of AISI 304 stainless steel dissolution process in conditions of intergranular corrosion, Electrochimica Acta 53 (13) (2008) 4387–4395.

[49] R. Tian, J. Sun, J. Wang, Study on behavior of plasma nitrided 316L in PEMFC working conditions, Int. J. hydrogen energy 33 (24) (2008) 7507–7512.

[50] A. Kraytsberg, M. Auinat, Y. Ein-Eli, Reduced contact resistance of PEM fuel cell's bipolar plates via surface texturing, J. Power Sources 164 (2) (2007) 697–703.

[51] R. Tian, J. Sun, Effect of pH value on corrosion resistance and surface conductivity of plasma–nitrided 304L bipolar plate for PEMFC, Int. J. Energy Res. 35 (9) (2011) 772–780.

[52] S.H. Lee, N. Kakati, J. Maiti, et al., Corrosion and electrical properties of CrN- and TiN-coated 316L stainless steel used as bipolar plates for polymer electrolyte membrane fuel cells, Thin Solid Films 529 (2013) 374–379.

[53] T. Ous, C. Arcoumanis, Degradation aspects of water formation and transport in proton exchange membrane fuel cell: A review, J. Power Sources 240 (2013) 558–582.

[54] L. Wang, J. Sun, P. Li, et al., Niobized AISI 304 stainless steel bipolar plate for proton exchange membrane fuel cell, J. Power Sources 208 (2012) 397–403.

[55] Y.G. Takei, T. Aoki, K. Sanui, et al., Dynamic contact angle measurement of temperature-responsive surface properties for poly (N-isopropylacrylamide) grafted surfaces, Macromolecules 27 (21) (1994) 6163–6166.